

Ce-modified SrFeO_{3-δ} for ethane oxidative dehydrogenation coupled with CO₂ splitting via a chemical looping scheme

Xin Tian, Chaohe Zheng, Haibo Zhao*

State Key Laboratory of Coal Combustion, School of Energy and Power Engineering, Huazhong University of Science and Technology, Wuhan 430074, PR China



ARTICLE INFO

Keywords:

Oxidative dehydrogenation
CO₂ utilization
Chemical looping
Perovskite-type oxygen carrier
Ce modification

ABSTRACT

The current study investigates Ce-modified SrFeO_{3-δ} oxygen carriers for oxidative dehydrogenation (ODH) of ethane coupled with CO₂ splitting in a chemical looping manner. During 39 cycles of redox testing over the sample of 0.2Ce/SrFeO₃, up to 29% ethane conversion and 82% ethylene selectivity are achieved, and the CO generation in the subsequent CO₂ splitting step is 0.25 mmol/g. XPS characterization results indicate decreased Fe²⁺/(Fe³⁺+Fe⁴⁺) ratio as well as increased active oxygen species proportion on the near-surface of Ce-modified samples, which are responsible for the improved activity of the 0.2Ce/SrFeO₃ in ethane ODH reaction. DFT calculations further reveal that the increased ODH activity of 0.2Ce/SrFeO₃ is due to the lower surface oxygen vacancy formation energy upon Ce promotion. Moreover, the higher resistance of lattice oxygen diffusion from the bulk to the surface is the main reason for the superior ethylene selectivity attained by the CO₂-regenerated sample than that by O₂ regeneration.

1. Introduction

The recent increase in shale gas production has the potential to reshape the energy pattern and chemical industry worldwide [1]. Ethylene, with a global demand of 175 million tons in 2018, is one of the most commonly used raw materials in numerous base chemicals production, which can be produced from the underutilized ethane (up to 10% depending on the origin) in shale gas [2,3]. Thermal steam cracking and direct dehydrogenation of ethane (C₂H₆ → C₂H₄ + H₂) are conventional routes for ethylene production, however, both of which are inevitably accompanied with high energy consumption (approximately 16 GJ/[t C₂H₄]), severe coke deposition, and significant CO₂ (1–1.2t CO₂/[t C₂H₄]) and NO_x emissions [4–8]. As an alternative, oxidative dehydrogenation (ODH) of ethane in the presence of O₂ (C₂H₆ + O₂ → C₂H₄ + H₂O) offers a new strategy for ethane conversion at much lower operating temperatures [9–11]. Nevertheless, the major limitation of this process is that the strong oxidizing property of O₂ usually leads to over-oxidation of ethane, resulting in inferior ethylene selectivity and a high CO₂ penalty [12]. To avoid these problems, the use of CO₂ as a mild oxidant under the scheme of tandem CO₂-assisted dehydrogenation of ethane (C₂H₆ + CO₂ → C₂H₄ + CO + H₂O) was further proposed [13–15]. Under such circumstance, an additional advantage is that CO can be co-produced from CO₂ dissociation, thus realizing ethane

valorization and CO₂ utilization simultaneously. Despite its various advantages, potential challenges still exist in CO₂-assisted ODH process. As a matter of fact, in order to enhance ethane conversion in this process, CO₂ is usually relatively excessive to C₂H₆ in the feeding gas stream [16, 17], leading to low CO₂ conversion and eventually increasing the burden of downstream products separation [18]. Recently, a similar but also quite different way for ethane and CO₂ co-utilization was put forward by Al-Mamoori et al. [19], in which the CO₂ reactant was provided by a CO₂ sorbent (K₂O-CaO, Na₂O-CaO, and CaO-based) instead of the CO₂ feeding stream, and the spent sorbent was then regenerated by capturing CO₂ from a flue gas stream. With this approach, 22% ethylene yield was attained and the CO₂ conversion was 14% (due largely to equilibrium limitations). To circumvent the equilibrium limitations of CO₂ conversion faced by conventional CO₂-assisted ODH process, Liu et al. [20] came up with a molten-carbonate-mediated ODH (MM-ODH) method to capture and utilize CO₂ for ethylene and CO co-production. Under the proposed MM-ODH scheme, super-equilibrium CO yield (89% at 770 °C) was eventually achieved by strategically partitioning CO₂-ODH reactions into gas and molten-salt phases.

Another potential way to achieve value-increment of ethane and CO₂ concurrently is through a chemical looping manner [21,22], i.e., chemical looping ethane oxidative dehydrogenation coupled with CO₂ splitting. As illustrated in Fig. 1, ethane is first converted into ethylene

* Corresponding author.

E-mail address: hzhao@mail.hust.edu.cn (H. Zhao).

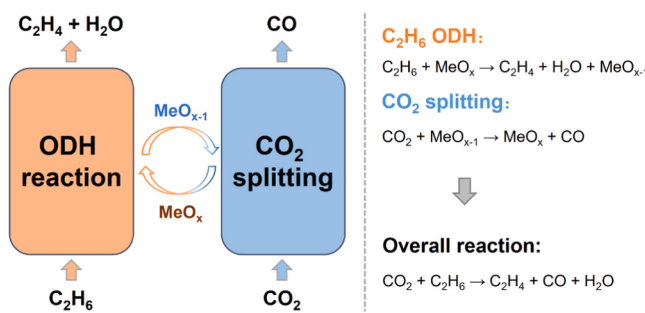


Fig. 1. A schematic view for the concept of ethane oxidative dehydrogenation (ODH) coupled with CO_2 splitting via chemical looping.

and H_2O in the ODH reactor, where the oxygen source required is provided by a selective oxygen carrier (MeO_x). Subsequently, in the CO_2 splitting reactor, the reduced oxygen carrier (MeO_{x-1}) regenerates itself by CO_2 exposure and CO is co-produced in the meantime. The overall reaction takes place within the two reactors is the same as that of the CO_2 -assisted ethane ODH process ($\text{C}_2\text{H}_6/\text{CO}_2$ co-feeding). One may argue that the requirement of two beds in chemical looping would make the reaction system more complicated and reduce the space-time yield to some extent. However, the main advantage of splitting the one-step $\text{C}_2\text{H}_6/\text{CO}_2$ conversion process into two sub-steps via chemical looping resides in the in situ separation of gaseous products (C_2H_4 and CO), as well as energy cascade utilization.

The key to realize the process of ethane ODH coupled with CO_2 splitting via chemical looping lies in the selection of a suitable oxygen carrier. To be more specific, the appropriate oxygen carrier should not only exhibit high selectivity to ethylene in the ethane ODH step, but it is also required to be effectively re-oxidized by CO_2 in the CO_2 splitting step and thus replenish its lattice oxygen [23,24]. These stringent requirements make the selection of a suitable oxygen carrier not a simple task. To date, investigation on the scheme of ethane ODH coupled with CO_2 splitting via chemical looping was quite rare [25]. On the other hand, plenty kinds of metal oxides have been investigated as oxygen carriers in the context of chemical looping oxidative dehydrogenation (CL-ODH) of ethane, using O_2 as the regeneration agent [26–31].

Na_2WO_4 promoted manganese-containing mixed oxides were reported to be effective oxygen carriers in CL-ODH of ethane, which obtained ethane conversion up to 76.5% with ethylene selectivity as high as 89.2% at 850 °C and 4500 h⁻¹ [32–35]. Under the working state, Na_2WO_4 formed a molten layer around the oxygen carrier, and this molten layer was believed to enhance ethylene production in two ways: i) decrease nonselective oxygen species; ii) facilitate lattice oxygen transport from/to the oxygen carrier substrate for selective H_2 combustion via the redox reaction of tungsten salt (likely between WO_4^{2-} and WO_3^-) [35]. Co and Mo co-doped Fe_2O_3 (Co: Mo = 0.3:0.7) prepared via the sol-gel method also showed superior selective H_2 combustion capability in CL-ODH of ethane, which gave 87.4% ethylene selectivity and 56.2% ethane conversion at 825 °C [36]. Nevertheless, due to the high temperature adopted in these studies, the superiority of oxygen carrier presence in lowering the dehydrogenation reaction temperature was not fully reflected. Gao et al. [37–39] proposed to modify $\text{La}_x\text{Sr}_{2-x}\text{FeO}_{4-\delta}$ with alkali metal (Li, Na, and/or K) salts for application in CL-ODH of ethane at much lower temperatures (≤ 700 °C). The best performance was attained by Li_2CO_3 (10 wt.%) promoted $\text{La}_x\text{Sr}_{2-x}\text{FeO}_{4-\delta}$, which exhibited 63.6% single-pass ethane conversion and 92.2% ethylene selectivity at 700 °C and 480 h⁻¹ [39]. The superior activity and selectivity of $\text{Li}_2\text{CO}_3/\text{La}_x\text{Sr}_{2-x}\text{FeO}_{4-\delta}$ was attributed to the molten layer formed by Li_2CO_3 in reaction, which stimulated the transport of active peroxide (O_2^{2-}) species formed on $\text{La}_x\text{Sr}_{2-x}\text{FeO}_{4-\delta}$ while suppressing non-selective sites. At 600 °C, Novotný et al. [40] evaluated the potential applicability of $\text{MoO}_3/\text{Fe}_2\text{O}_3$ in CL-ODH of ethane. However, the highest ethane conversion attained was less than

6% and a large amount of CO_x (selectivity higher than 37%) was generated in reaction, which made this material uncompetitive.

To the best of our knowledge, the only one relevant study on ethane ODH coupled with CO_2 splitting via chemical looping in literatures was conducted by Jeong et al. [25] Using Fe (at varying loadings, 1–20 wt. %) impregnated rutile TiO_2 nanoparticle as oxygen carrier, the highest ethylene selectivity (91.1%) and ethane conversion (9.7%) was obtained by $\text{Fe}(5)/\text{TiO}_2$, together with a maximum amount of 2.02 mmol/g CO generation in the subsequent CO_2 splitting step. It is worth noting that, in order to strike a satisfactory balance between ethylene selectivity and CO_2 conversion, temperature swing was required for the ODH step (550 °C) and CO_2 splitting step (700 °C) in their reaction system [25]. Otherwise, a higher ODH temperature would result in severe coke deposition, while a lower CO_2 splitting temperature lead to low CO_2 conversion and slow regeneration rate of the reduced oxygen carrier. However, the temperature swing requirement made the reaction system rather complicated, and should be avoided in real application.

Ceria has been widely investigated as catalyst for $\text{C}_2\text{H}_6/\text{CO}_2$ co-feeding ODH reaction, owing to its tunable redox property and catalytic activity, high oxygen carrying capacity, as well as abundant oxygen vacancy [41–44]. The oxygen vacancies possessed by CeO_2 can on one hand increase the mobility of lattice oxygen so as to facilitate ethane conversion, and on the other hand activate CO_2 to generate active oxygen species to remove potential carbon deposits. In this work, Ce-modified $\text{SrFeO}_{3-\delta}$ synthesized by the sol-gel method was evaluated as oxygen carrier in the context of ethane ODH coupled with CO_2 splitting via a chemical looping manner. The proper amount of Ce addition was found to not only facilitate perovskite phase ($\text{SrFeO}_{3-\delta}$) formation in sample preparation, but also increase the activity of the attained oxygen carrier in ethane ODH reaction. The effects of different regeneration agents (CO_2 vs. O_2) on the physicochemical properties of the re-oxidized oxygen carrier as well as on its subsequent ethane ODH performance were for the first time investigated under the chemical looping scheme. The main factors that affect the ethylene selectivity of different oxygen carriers were unveiled on the basis of reaction testing and characterization results, as well as density functional theory calculation (DFT).

2. Experimental and computational section

2.1. Oxygen carrier synthesis

The $\text{SrFeO}_{3-\delta}$ -based oxygen carriers used in this work were all prepared by a simple sol-gel method described elsewhere [29,36]. Briefly, stoichiometric amounts of $\text{Sr}(\text{NO}_3)_2$ (Aladdin, 99.5% purity), $\text{Fe}(\text{NO}_3)_3 \cdot 9\text{H}_2\text{O}$ (Sinopharm, ≥98.5% purity), and $\text{Ce}(\text{NO}_3)_3 \cdot 6\text{H}_2\text{O}$ (Sinopharm, ≥99.0% purity) were dissolved in deionized water (the molar ratio of Ce/Sr for the Ce-modified sample was 0.2:1 or 0.4:1) and electromagnetically stirred on a hot plate at 40 °C. Citric acid ($\text{C}_6\text{H}_8\text{O}_7 \cdot \text{H}_2\text{O}$, Sinopharm, ≥99.5% purity) at a molar ratio of 2.5:1 to the total metal ions (Sr^{2+} , Fe^{3+} , Ce^{3+}) was then added into the solution. The solution was kept stirring at 450 rpm and 40 °C for 30 min. Afterwards, ethylene glycol ($\text{C}_2\text{H}_6\text{O}_2$, Sinopharm, ≥99.5% purity) was introduced into the mixture to promote gel formation at a molar ratio of 1.5:1 to citric acid. The attained solution was heated to 80 °C under continuous stirring until a viscous gel formed, and then dried overnight in an oven to remove moisture at 120 °C. The dried precursor was finally calcined in air atmosphere at 850 °C for 4 h (unless otherwise specified) to attain the fresh oxygen carriers. For the sample without Ce modification, 850 °C was found to be insufficient to attain pure perovskite phase. Thus, in another batch, calcination at 1200 °C for 12 h was conducted over the unmodified sample. Eventually, four samples were attained, and they were named as SrFeO_3 , SrFeO_3 (1200 °C), 0.2Ce/ SrFeO_3 , and 0.4Ce/ SrFeO_3 , respectively. All samples were ground and sieved into the size range of 250–450 μm for reaction testing.

2.2. Testing conditions

The redox reaction tests were conducted in a 4 mm I.D. fixed-bed quartz U-tube reactor. The reactor was embedded in a furnace and electrically heated. The reaction temperature was monitored by a K-type thermocouple near the sample bed, and controlled by a PID component. In each test, 700 mg (approximately 0.4 mL in volume) of oxygen carrier was loaded into the U-tube reactor, with Al_2O_3 grit (1.0–1.5 mm) added into the void space to limit dead volume in the heated zone. For comparison, control experiments with only Al_2O_3 grit as the bed material were also conducted. The gas flow rates and compositions were controlled by mass flow controllers and an automated valve switching system. The samples were polished at 800 °C for three redox cycles comprising a 2 min reduction step of 25 vol.% H_2/Ar (total flowrate of 40 mL/min) and a 9 min oxidation step of 25 vol.% CO_2/Ar (or 25 vol.% O_2/Ar , total flowrate of 40 mL/min).

During the formal reaction testing, the samples were evaluated at three different temperatures (700 °C, 725 °C, and 750 °C) and three different gas hourly space velocities (GHSV: 3000 h^{-1} , 4500 h^{-1} , and 6000 h^{-1}). Note that, the total volume of ethane fed in each test was kept the same of 17.5 mL at different GHSV, and the GHSV of 6000 h^{-1} corresponded to a total flow rate of 40 mL/min. In the tests, the duration of the ethane ODH step was 3.5 min (at 3000 h^{-1} , unless otherwise specified) and the CO_2 splitting step was 9 min (or O_2 oxidation for 5 min). A 5 min purge step with pure Ar flow was introduced between each ethane ODH step and CO_2 splitting (or O_2 oxidation) step. The outlet gas products were observed by an online mass spectrometer (Hiden HPR-20, UK). For each test condition, 5 redox cycles were conducted and the mass data at the 4th cycle were used for analysis. As there was negligible coke or tar formation under all isothermal test conditions (no obvious CO/CO_2 signal detected in the O_2 oxidation step), the conversion of ethane and selectivity to all carbonaceous products were calculated on a carbon basis. The total amount of hydrogen generated and consumed to H_2O were calculated by hydrogen mass balance of all detected products. Additional information and formulas for conversion, selectivity, yield, and hydrogen conversion can be found in [Supporting information](#).

2.3. Characterization techniques

X-ray diffraction (XRD) was employed to probe the crystal phases of both the as-prepared and cycled oxygen carriers, using a Bruker D8 Advance X-ray diffractometer with Cu K α ($\lambda = 0.1542 \text{ nm}$) radiation operating at 40 kV and 40 mA. Scans were performed stepwise with a 0.02° step size and holding time of 3 s in a 2 θ range of 20–80°. The crystal phases of the samples were determined by employing JADE 6.0 using the database of PDF-2004.

X-ray photoelectron spectroscopy (XPS) measurements were conducted on a Thermo ESCALAB 250xi to determine the near-surface elemental compositions as well as chemical states of the samples, with an Al anode (1486.6 eV) as the excitation source. For each sample, XPS narrow scans were taken for all metal cations (Sr 3d, Fe 2p, and Ce 3d), C 1 s, and O 1s. The Avantage program (ThermoFisher Scientific Inc., USA) was used to analyze the XPS patterns, with the adventitious C 1s peak at 284.6 eV used for binding energy calibration.

Nitrogen sorption isotherms of both the fresh and cycled samples were obtained at 77 K with a physisorption apparatus (Micromeritics ASAP 2020, USA) via a multipoint physical adsorption measurement. Prior to the measurements, all samples were degassed overnight at 473 K under vacuum. The specific surface area was calculated by the Brunauer–Emmett–Teller (BET) method.

The microstructure of samples was characterized using TEM (Tecnai G² F30, FEI) coupled with energy-dispersive spectroscopy (EDS, EDAX Genesis) at an accelerating voltage of 300 kV.

C_2H_6 -TPR (temperature programmed reaction) tests were carried out in the quartz U-tube reactor as described before. In each test, samples of

700 mg (250–450 μm) were loaded into the U-tube reactor. As a control, thermal blank C_2H_6 -TPR test over inert Al_2O_3 grit was also conducted. Before formal testing, the sample was pre-treated at 800 °C for three redox cycles, comprising of a 2 min H_2 reduction step (25 vol.% H_2/Ar , 40 mL/min) and a 9 min oxidation step (using either 25 vol.% O_2/Ar or 25 vol.% CO_2/Ar , 40 mL/min) in each cycle. After cooling down to room temperature, the samples were heated to 200 °C at 10 °C/min and held there for 10 min under pure Ar flow (40 mL/min). Then, the gas flow was switched to 5 vol.% $\text{C}_2\text{H}_6/\text{Ar}$ (total flowrate of 40 mL/min) and the reactor was slowly heated to 800 °C at a heating rate of 5 °C/min. Gas products during the TPR test were analyzed by the Hiden HPR-20 mass spectrometer.

O_2 -TPD (temperature programmed desorption) and H_2 -TPR tests were undertaken in a TGA produced by the Setaram Instrumentation (SETSYS EVO16) [45]. Before the test, the sample was pre-treated following the same procedure as described above in the C_2H_6 -TPR. In the formal test, the sample (~20 mg, <0.1 mm) was placed in an alumina crucible and first heated to 200 °C at a ramping rate of 10 °C/min in pure Ar (60 mL/min). After 10 min of holding at 200 °C, the reaction chamber was heated to 850 °C at 5 °C/min, in either H_2/Ar (H_2 -TPR, 5 vol.% H_2 at 60 mL/min) or pure Ar (O_2 -TPD, 60 mL/min). The mass change of the sample was recorded by a computer for further data analysis.

2.4. Computational details

The calculations were conducted with the spin-polarized density functional theory (DFT) method using the Cambridge Serial Total Energy Package (CASTEP) [46]. The Perdew–Burke–Ernzerhof (PBE) exchange-correlation function was performed, and the Hubbard GGA+U value of 3.5 eV was used to amend the Fe 3d orbital. The cutoff energy was set to 370 eV to describe a plane-wave basis set. Monkhorst–Pack k -point meshes of $6 \times 6 \times 6$ and $3 \times 3 \times 1$ were chosen for the lattice cell and slab calculations, respectively. The lattice parameters of the optimized SrFeO_3 cell ($a=b=c=3.855$) were in good agreement with experimental values ($a=b=c=3.851$) [47]. A five-layer SrFeO_3 (001) surface (bottom three layers fixed) with a vacuum space of 15 Å was constructed [48,49]. The convergence criterion for the total energy, maximum interatomic force, and displacement were 1.0×10^{-5} eV/atom, 0.03 eV/Å, and 0.001 Å, respectively. More details of constructed SrFeO_3 models can be found in [Fig. S9 of Supporting information](#).

3. Characterization and redox reaction performance evaluation

3.1. Structural characterization

The crystalline phase of as prepared SrFeO_3 , SrFeO_3 (1200 °C), 0.2Ce/ SrFeO_3 , and 0.4Ce/ SrFeO_3 were characterized by powder XRD, as shown in [Fig. 2a-d](#). The results indicate that calcination at 850 °C for 4 h is not sufficient to form pure $\text{SrFeO}_{3-\delta}$ phase for the sample without Ce modification ([Fig. 2a](#)). By increasing the calcination temperature to 1200 °C as well as the duration to 12 h, monophasic $\text{SrFeO}_{3-\delta}$ (PDF# 39-0954) phase is finally attained for the unmodified sample ([Fig. 2b](#)). The unpromoted $\text{SrFeO}_{3-\delta}$ shows up major peaks at 32.8°, 40.4°, 46.9°, 58.5°, 68.7°, and 78.2°, corresponding to (110), (111), (200), (211), (220), and (310) planes, respectively. With respect to the two Ce-modified samples, $\text{SrFeO}_{3-\delta}$ phase can be well-formed upon 850 °C calcination for 4 h. In addition, characteristic peaks indexable to CeO_2 (PDF# 34-0394) are also observed in Ce-modified samples ([Fig. 2c, d](#)). With these results, it may be deduced that the introduction of Ce can facilitate $\text{SrFeO}_{3-\delta}$ perovskite phase formation at much “milder” calcination conditions. Moreover, there is slight shift for the main characteristic peak of $\text{SrFeO}_{3-\delta}$ after Ce modification (changed from 32.8° to 32.7°, as indicated by the enlarged view of the scan between 31.5°–33.5°), suggesting enlargement of the unit cell [50], which was further verified by refining the XRD spectra (with a unit cell volume of

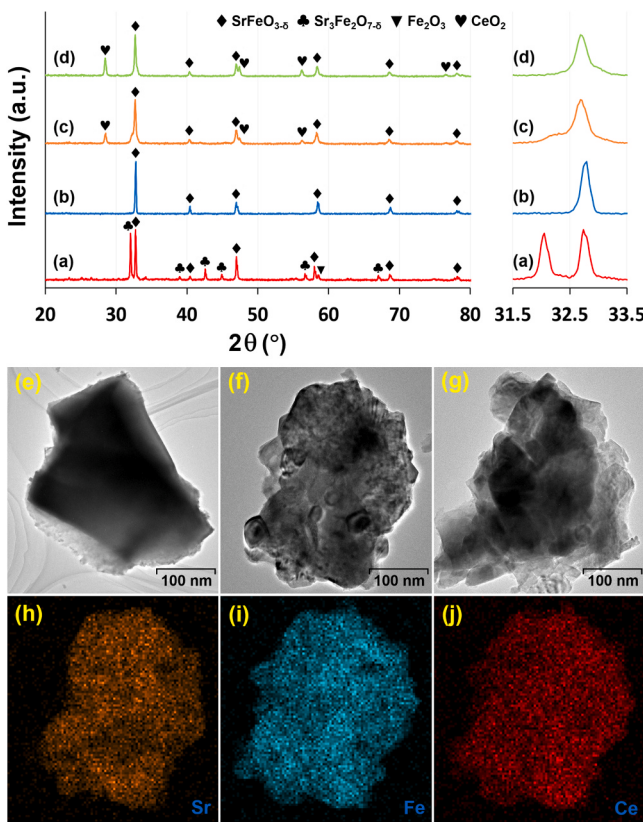


Fig. 2. Structural characterizations for the as-prepared samples. (a-d) XRD patterns of SrFeO₃, SrFeO₃ (1200 °C), 0.2Ce/SrFeO₃, and 0.4Ce/SrFeO₃, respectively. (e-g) TEM images of SrFeO₃ (1200 °C), 0.2Ce/SrFeO₃, and 0.4Ce/SrFeO₃, respectively. (h-j) EDS mapping of 0.2Ce/SrFeO₃. Notes: the sample of SrFeO₃ (1200 °C) was calcined at 1200 °C for 12 h, while all the others were calcined at 850 °C for 4 h.

58.49 Å³ and 58.88 Å³, respectively). By the way, Ce can be incorporated into the A site of the SrFeO_{3-δ} lattice [51,52], which might be also responsible for the peak shift of the perovskite upon Ce introduction. TEM characterizations were further conducted over fresh SrFeO₃ (1200 °C), 0.2Ce/SrFeO₃, and 0.4Ce/SrFeO₃ samples, as shown in Fig. 2e-g, respectively. As indicated, well-developed porous structure can be observed on the surface of both 0.2Ce/SrFeO₃ and 0.4Ce/SrFeO₃, which is beneficial for gas-solid reactions. While for the sample of SrFeO₃ (120 °C), a rather dense microstructure is attained. This is mainly due to the high-temperature annealing procedure adopted in sample preparation, and BET results shown in Supporting information (Table S1) further indicate quite small specific surface area of the fresh SrFeO₃ (1200 °C) sample (0.63 m²/g). The elemental mapping results of 0.2Ce/SrFeO₃ by EDS (Fig. 2h-j) suggest that all elements (Sr, Fe, Ce) are uniformly dispersed in the as-prepared sample. Additional TEM-EDS results for both SrFeO₃ (1200 °C) and 0.4Ce/SrFeO₃ can be found in Fig. S1 of Supporting information.

3.2. Ethane ODH and CO₂ splitting reaction results

The reaction performance of all as-prepared samples for chemical looping ethane ODH coupled with CO₂ splitting were evaluated through isothermal tests. Fig. 3a displays the ethane conversion and ethylene selectivity attained by different samples in the ethane ODH step. The dashed lines in the figure demonstrate the constant contours of ethylene yield, and arrows point in the direction of increasing temperature. The carbon balance for all tests is calculated to be in the range of 97–102%. Significant increase of ethane conversion is observed for all oxygen carriers in comparison with that of thermal blank, as ascribed to the

donation of lattice oxygen from oxygen carriers that facilitates the ODH reaction to certain degrees. With the increase of temperature, a higher ethane conversion as well as a lower ethylene selectivity are attained for all samples. This is expected, since both ethane cracking reaction as well as the activity of lattice oxygen in oxygen carrier will be intensified at higher temperatures [53]. For further comparison, Fig. 3b specifies the products distribution over different samples at 725 °C and 3000 h⁻¹ in the ethane ODH step. The evolution profiles of gaseous products during a complete ethane ODH and CO₂ splitting (or O₂ oxidation) cycle for each sample are presented in Fig. S2 of Supporting information. Among all oxygen carriers, 0.2Ce/SrFeO₃ shows the highest activity towards ethane conversion and moderate ethylene selectivity; while SrFeO₃ (1200 °C) shows the highest ethylene selectivity but the poorest activity. A higher Ce doping ratio shows no further improvement in activity or selectivity for the attained sample (i.e., 0.4Ce/SrFeO₃). These results indicate that proper amount of Ce introduction is effective for enhancing the ODH activity of the SrFeO_{3-δ} substrate. The reason for the varied ODH performance of different samples will be detailed in later sections. Eventually, the ethylene yield of 0.2Ce/SrFeO₃ is over twice as that as thermal blank at temperatures lower than 725 °C, while maintaining ethylene selectivity higher than 81%. The lattice oxygen donated by 0.2Ce/SrFeO₃ in ODH reaction is calculated to be 0.37 wt.% of the total mass of the sample. By the way, the sample of 0.2Ce/SrFeO₃ (O₂) regenerated by O₂ tends to be less selective (to ethylene) compared to the sample of 0.2Ce/SrFeO₃ (regenerated by CO₂), while no significant increase in activity is observed. The reaction data clearly demonstrate the superiority of CO₂ regeneration of the reduced sample, and the underlying mechanism will be revealed by both XPS analysis and DFT calculation in the sections that follow. More detailed reaction testing results of different samples are found in Table S2 of Supporting information. It is worth noting that most of the samples showed sufficient good cyclic stability in redox reaction, as both confirmed by the reaction testing data and XRD results of the used samples shown in Fig. S3 of Supporting information. But it is not the case for the sample of SrFeO₃, which showed obvious activity degradation in redox cycling. This is mainly attributed to the significant generation of inactive SrCO₃ phase in redox reaction (Fig. S3a). Actually, Fig. S2a indicates that the amount of CO₂ consumed is much larger than CO generation in the CO₂ splitting step for the SrFeO₃, due to the occurrence of carbonation reaction therein.

The effect of GHSV on the ethane ODH performance of 0.2Ce/SrFeO₃ is illustrated in Fig. 3c, and further relevant reaction data is summarized in Table S3. As it can be seen, an increase in GHSV leads to an increase in ethylene selectivity but a decrease in both ethane conversion and in situ H₂ conversion. This is understandable, since a decrease in gas residence time weakens the contact between ethane and oxygen carrier (resulting in lower ethane conversion), as well as alleviates the sequential combustion of ethylene product (leading to higher ethylene selectivity). The in situ H₂ conversion (to water) in the ethane ODH step is beneficial from both standpoints of breaking the thermodynamic equilibrium of ethane conversion and generating oxygen vacancies for subsequent CO₂ splitting reaction. In fact, it is evident that the CO generation in the CO₂ splitting step is highly related to the reaction extent of the ethane ODH step, as indicated by the results shown in Fig. S2a-d of Supporting Information. Fig. 3d shows the evolution profiles of CO₂ and CO as well as the instantaneous CO₂ conversion over 0.2Ce/SrFeO₃ in the CO₂ splitting half cycle. Generally, the reduced sample can almost completely regenerate itself by CO₂ in 6 min. In addition, the instantaneous CO₂ conversion during the first 1 min is over 60%. The average CO₂ conversion within the first 1.5 min, 3 min, 6 min, and 9 min of the CO₂ splitting step was further calculated as 54.9%, 27.7%, 13.4%, and 9.1%, respectively. This result is better than that attained by Jeong et al. [25], of which the CO₂ conversion never exceeded 10% within 1 h of reaction. The total amount of CO generated was calculated to be 0.25 mmol/g over the reduced 0.2Ce/SrFeO₃ at 725 °C (it was 2.02 mmol/g_{cat} in the work of Jeong et al. [25]). More details on CO generation of different samples in the CO₂ splitting step can be found in Table S4 of Supporting

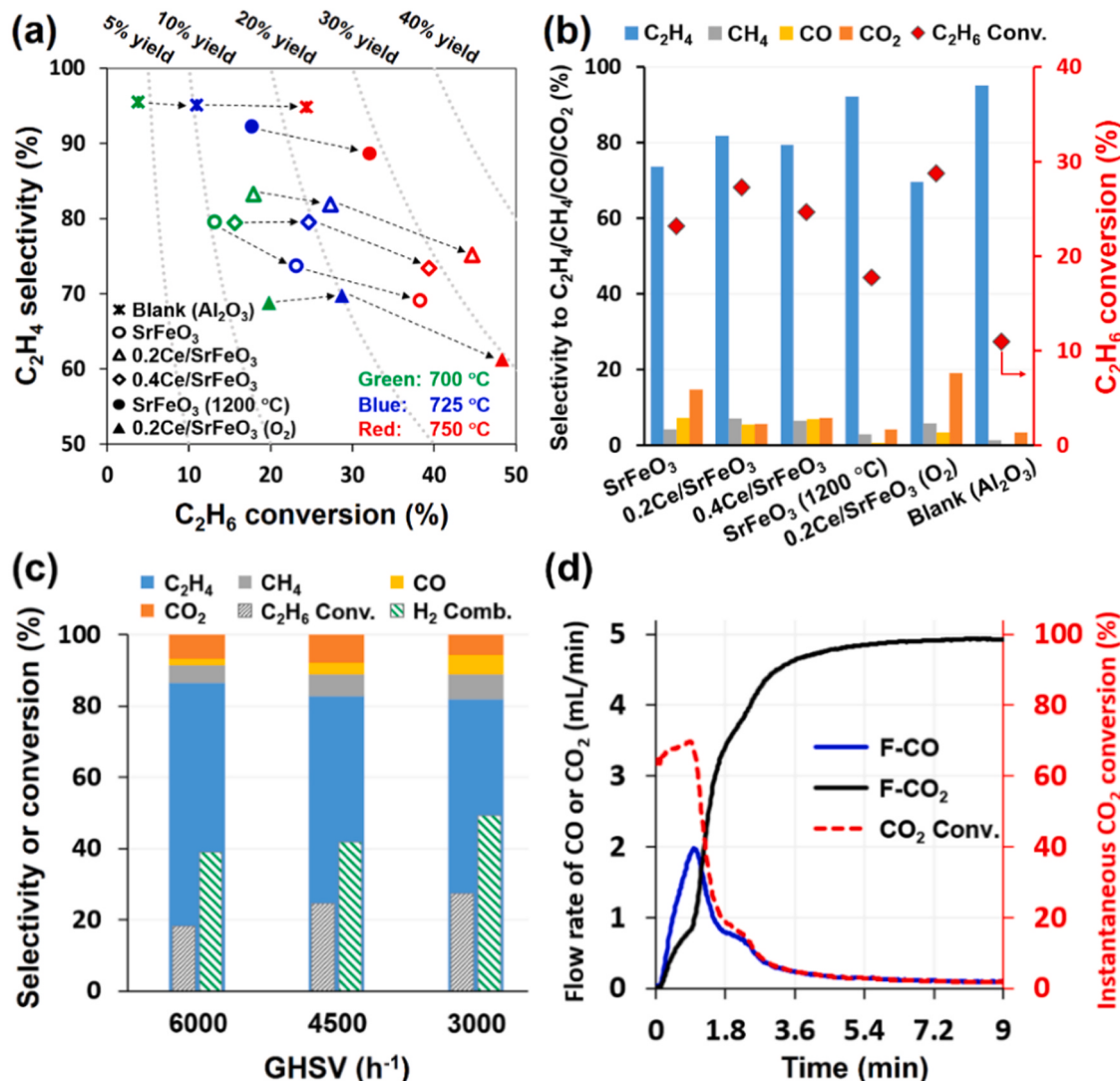


Fig. 3. Redox testing of different oxygen carriers for chemical looping ethane ODH coupled with CO₂ splitting. (a) Temperature effect on the reaction performance of different oxygen carriers (as well as thermal blank) in the ethane ODH step: GHSV, 3000 h⁻¹. (b) Carbonaceous products distribution over different oxygen carriers (as well as thermal blank) in the ethane ODH step: temperature, 725 °C; GHSV, 3000 h⁻¹. (c) GHSV effect on the reaction products distribution of 0.2Ce/SrFeO₃ in the ethane ODH step: temperature, 725 °C. (d) Instantaneous CO₂ conversion and CO generation over the reduced 0.2Ce/SrFeO₃ in the CO₂ splitting step: temperature, 725 °C; GHSV, 3000 h⁻¹. **Notes:** the sample of SrFeO₃ (1200 °C) was calcined at 1200 °C for 12 h, while all the others were calcined at 850 °C for 4 h; the 0.2Ce/SrFeO₃ (O₂) was regenerated by O₂, while all the others were by CO₂.

information. Generally, a higher reaction temperature will significantly increase the CO generation in the CO₂ splitting step (Table S4), but decrease the ethylene selectivity in the ethane ODH step at the same time (Fig. 3a). This is expected, at a higher reaction temperature, the ethylene selectivity decreases due to the enhanced over-oxidation activity of the oxygen carrier, and the increased CO generation in the CO₂ splitting step is ascribed to the higher reduction degree of oxygen carrier achieved in the ODH step.

3.3. Cyclic stability

To evaluate the redox durability of the 0.2Ce/SrFeO₃ sample, the ethane ODH/CO₂ splitting cycles were continuously conducted for 39 times at 725 °C and 3000 h⁻¹, as shown in Fig. 4a-b. In the ethane ODH step, ethylene selectivity of 82.0% together with 29.1% ethane conversion were attained without obvious decay after 39 cycles (Figs. S4 and S5). The ethylene yield attained by 0.2Ce/SrFeO₃ was over two times higher than that of thermal blank (23.8% vs. 10.4%). With respect to the CO₂ splitting step, the CO generation maintained at 0.25 mmol/g

with stable peak CO₂ conversion of ca. 69.4%. The structural stability of 0.2Ce/SrFeO₃ was further confirmed by XRD results (Fig. S6), which nearly identical XRD patterns were attained for the as-prepared and cycled samples. It should be noted that the peak intensity of CeO₂ weakened to a certain extent in the cycled sample, which can be attributed to the gradual incorporation of Ce into the SrFeO_{3-δ} lattice during redox cycling [50]. Furthermore, a small peak at $2\theta = 25.2^\circ$ was observed in the XRD patterns of the cycled sample, corresponding to SrCO₃. TEM-EDS results (Fig. S7) show that porous structure of the cycled sample was well-maintained after 39 cycles, and all elements were still evenly distributed within the particle. A slight decrease in BET surface area was observed for the cycled sample, together with an enlargement of pore size (Table S1). Overall, these results demonstrate the sufficiently good cycling stability of 0.2Ce/SrFeO₃ in chemical looping ethane ODH coupled with CO₂ splitting.

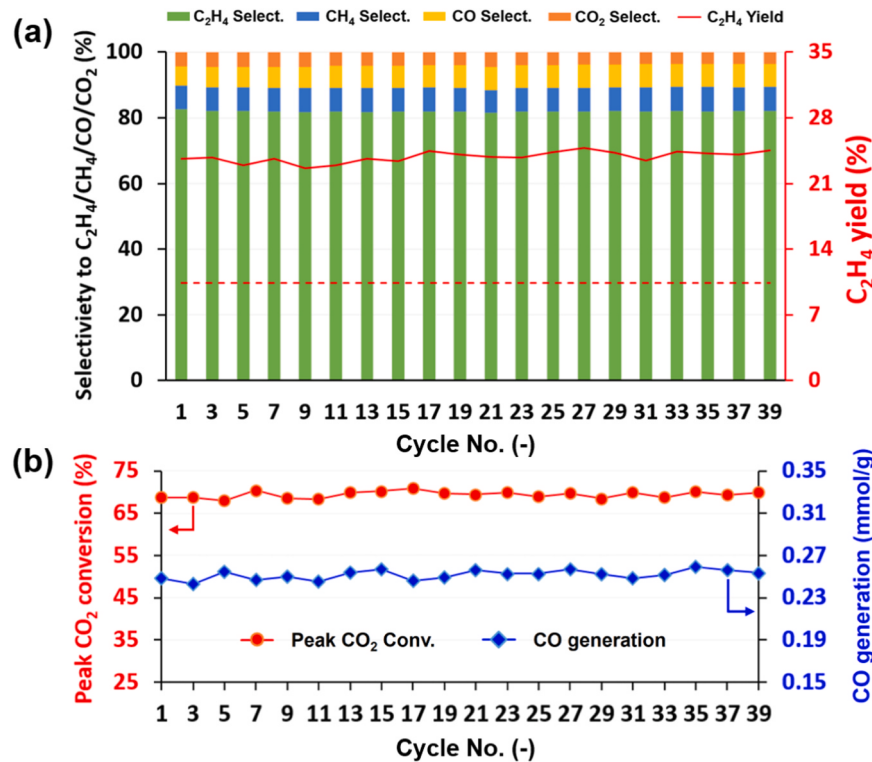


Fig. 4. Redox stability of 0.2Ce/SrFeO₃. (a) The carbonaceous products distribution and ethylene yield (thermal background ethylene yield is given as a red dash line) in the ethane ODH step for 39 cycles. (b) CO productivity and peak CO₂ conversion attained in the CO₂ splitting step for 39 cycles. Temperature, 725 °C; GHSV, 3000 h⁻¹.

4. Mechanistic investigation and discussions

4.1. C₂H₆-TPR

Ethane TPR tests were performed to investigate the ODH reaction pathway, as well as to analyze the production of reaction products as a function of reaction temperature. The instantaneous flow rates of gaseous products generated within the C₂H₆-TPR tests over different samples are shown in Fig. 5a–e, and the corresponding onset reaction temperatures are summarized in Fig. 5f. It is noted that the onset reaction temperatures for all oxygen carriers (except SrFeO₃ (1200 °C)) were well below that of thermal blank. These results indicate that the presence of oxygen carrier exhibits certain catalytic activation of ethane on the surface of the oxide. Comparatively, the SrFeO₃ (1200 °C) tended to be less reactive and showed little catalytic effect on ethane conversion, which had a very similar onset reaction temperature as that of thermal blank (698 °C vs. 699 °C, Fig. 5f). It is also noted that nearly identical lines of H₂ and C₂H₄ flow rates are observed in the test of thermal blank (Fig. 5a), while the H₂ flow rate line is under that of C₂H₄ at the beginning of the test with the presence of an oxygen carrier (Fig. 5b–e). Such findings indicate that the presence of oxygen carrier can achieve a certain degree of in situ H₂ conversion within the ethane ODH reaction. In addition, different regeneration agents (CO₂ vs. O₂) did significantly affect the ODH reaction performance of the re-oxidized oxygen carrier, as indicated by the results of 0.2Ce/SrFeO₃ and 0.2Ce/SrFeO₃ (O₂) shown in Fig. 5b and d, respectively. To be more specific, the reaction of CO₂ regenerated 0.2Ce/SrFeO₃ was initiated at 620 °C, and high ethylene selectivity was maintained till the temperature reached 750 °C. With respect to the O₂ regenerated 0.2Ce/SrFeO₃ (O₂), CO₂ signal appeared at temperature as low as 224 °C due to the oxidation of ethane by nonselective chemisorbed oxygen species on the oxide surface. Subsequently, a second “onset” of reaction occurred at 647 °C, as attributed to the participation of selective lattice oxygen from the oxide bulk. These results agree well with that of the isothermal test

over 0.2Ce/SrFeO₃ (O₂) in ethane ODH reaction, which a sharp CO₂ peak emerged at the beginning of the reaction and then decreased gradually as the reaction proceeded (Fig. S2e). For the sample of 0.4Ce/SrFeO₃, similar gaseous products evolution profiles as those of 0.2Ce/SrFeO₃ are observed, regardless of its higher onset reaction temperature (661 °C vs. 620 °C). Moreover, higher CO selectivity is found over the sample of 0.4Ce/SrFeO₃ as compared to that of 0.2Ce/SrFeO₃.

4.2. XPS analysis

For the investigated SrFeO_{3-δ} system in ethane ODH reaction, the transformation in Fe valance state is considered to be associated with lattice oxygen donation, which is responsible for the activity of the oxygen carrier. On the other hand, the selectivity of the oxide towards ethane conversion is largely affected by the properties of near-surface oxygen species. To elucidate the varied reaction performance of different oxygen carriers in the ethane ODH step, the O 1s and Fe 2p XPS spectra of the used SrFeO₃ (1200 °C), 0.2Ce/SrFeO₃, 0.4Ce/SrFeO₃, and 0.2Ce/SrFeO₃ (O₂) were examined in detail, as shown in Fig. 6. Furthermore, in Supporting information, the detailed analysis results of O 1s and Fe 2p_{3/2} spectra for the four samples are summarized in Table S5, and the Sr 3d as well as Ce 3d XPS scans are illustrated in Fig. S8.

As it can be seen in Fig. 6, the Fe 2p spectra is featured with a double-peaked spectrum and two small satellite peaks, indicating the existence of multiple components of Fe cations with different chemical valence states. The double-peaked spectrum is related to inner Fe 2p_{3/2} (~710.4 eV) and Fe 2p_{1/2} (723.8 eV) levels. For each sample, three peaks at binding energies around 709.7–710.3 eV, 711.2–712.4 eV, and 714.3–715.5 eV can be attained through the deconvolution of Fe 2p_{3/2}, corresponding to Fe²⁺, Fe³⁺, and Fe⁴⁺ species, respectively [50,54]. The detailed XPS analysis results of Fe 2p_{3/2} shown in Table S5 indicate that the introduction of Ce onto the SrFeO_{3-δ} system would affect the distribution of near-surface Fe species in valence states. To be more

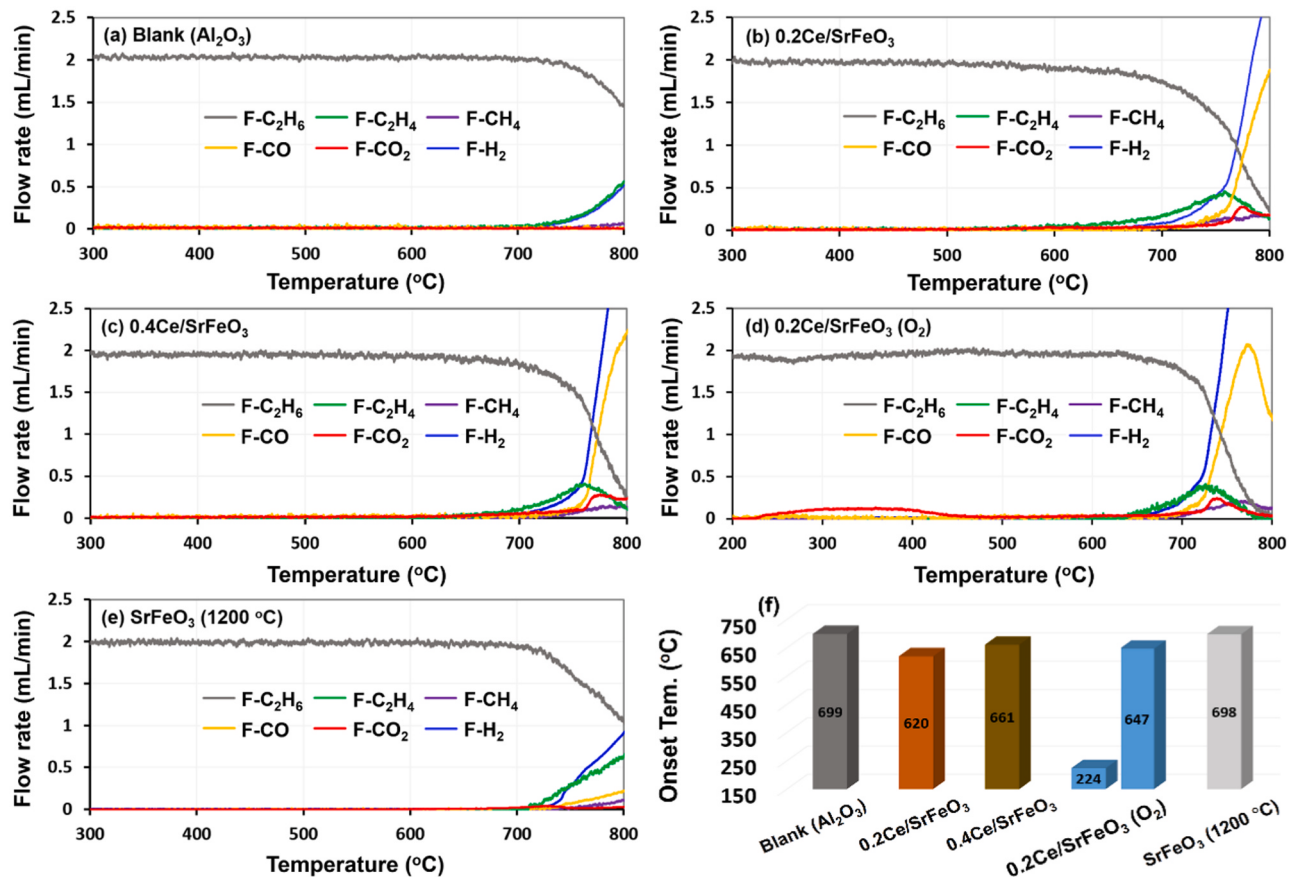


Fig. 5. Results from C₂H₆-TPR over four oxygen carriers and accompanying thermal background. (a) Thermal blank (Al₂O₃). (b) 0.2Ce/SrFeO₃. (c) 0.4Ce/SrFeO₃. (d) 0.2Ce/SrFeO₃ (O₂). (e) SrFeO₃ (1200 °C). (f) The onset reaction temperature of different samples in C₂H₆-TPR test. Conditions: temperature range, 200–800 °C; heating rate, 5 °C/min; GHSV, 6000 h⁻¹ (total flowrate of 40 mL/min); ethane concentration, 5 vol.%. Notes: the sample of SrFeO₃ (1200 °C) was calcined at 1200 °C for 12 h, while all the others were calcined at 850 °C for 4 h; the 0.2Ce/SrFeO₃ (O₂) was regenerated by O₂, while all the others were by CO₂.

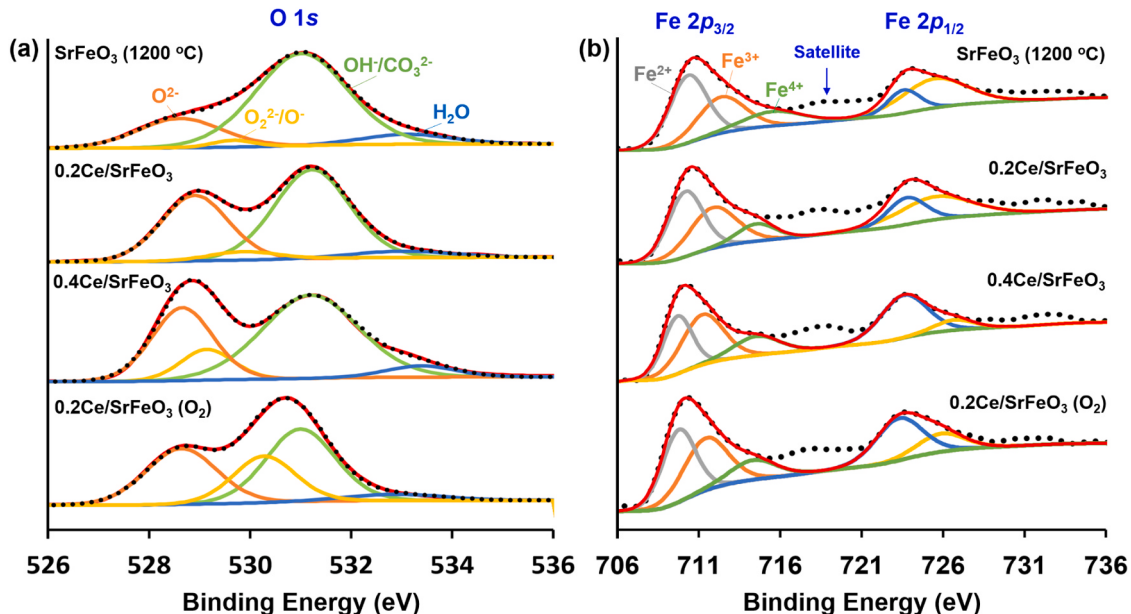


Fig. 6. Detailed O 1s (a) and Fe 2p XPS (b) scan of the used samples. Samples including SrFeO₃ (1200 °C), 0.2Ce/SrFeO₃, 0.4Ce/SrFeO₃, and 0.2Ce/SrFeO₃ (O₂). All samples were in oxidation state. Notes: the sample of SrFeO₃ (1200 °C) was calcined at 1200 °C for 12 h, while all the others were calcined at 850 °C for 4 h; the 0.2Ce/SrFeO₃ (O₂) was regenerated by O₂, while all the others were by CO₂.

specific, a clear decrease of the $\text{Fe}^{2+}/(\text{Fe}^{3+}+\text{Fe}^{4+})$ ratio can be seen upon Ce modification, and similar result was also observed in previous publication [50]. The increase of the overall valence state of Fe in $\text{SrFeO}_{3-\delta}$ should be compensated by the decrease of δ value associate with O^{2-} , considering that the potentially incorporated Ce^{4+} also had a higher valance state than Sr^{2+} . From this respect, one may argue that a high proportion of Ce modification would be better, as it increases the oxygen carrying capacity of the resulted $\text{Sr}_{1-x}\text{Ce}_x\text{FeO}_{3-\delta}$ system. But it should be noted that the highest tolerance ratio of Ce/Sr in the $\text{Sr}_{1-x}\text{Ce}_x\text{FeO}_{3-\delta}$ system is 0.15/0.85 [50,51]. In addition, O_2 -regenerated 0.2Ce/SrFeO₃ (O_2) also decreased the near-surface $\text{Fe}^{2+}/(\text{Fe}^{3+}+\text{Fe}^{4+})$ ratio of the sample in comparison to that of CO_2 -regenerated 0.2Ce/SrFeO₃ (Table S5). This is understandable in view of the much stronger oxidizing property of O_2 than that of CO_2 .

With respect to the deconvolution of O 1s spectra, two major peaks and two minor peaks are observed for all samples. The major peak with lower binding energy at around 528.6–528.9 eV is assigned to lattice oxygen species, and the second major peak locates around 531.0–531.2 eV can be assigned to hydroxide (OH^-) and/or carbonate (CO_3^{2-}) species [37,38]. A minor intermediate peak appears at around 529.2–530.2 eV is associated with electrophilic oxygen species [55], and the other minor peak with the highest binding energy at about 533.1 eV is attributed to adsorbed molecular water on the surface of the oxide [56]. In the ethane ODH reaction, both lattice oxygen and surface electrophilic oxygen species can contribute to ethane conversion, but to different directions: the electrophilic oxygen species are considered to be nonselective and are responsible for deep oxidations; while lattice oxygen species are usually selective and are beneficial for ethylene production [32,35]. By comparing the O 1s spectra of the four samples, it is evident that the relative intensity of the first major peak corresponding to lattice oxygen was obviously suppressed for the sample of SrFeO_3 (1200 °C), which agrees well with its worst activity towards ethane conversion (Fig. 3b). With respect to the 0.2Ce/SrFeO₃ and 0.4Ce/SrFeO₃, similar relative amounts of active oxygen species (lattice oxygen and electrophilic oxygen species) were detected (40.8% vs. 37.5%, Table S5), but 0.4Ce/SrFeO₃ contained a higher proportion of electrophilic oxygen species. This result is consistent with the superior reaction performance (both in activity and selectivity) of 0.2Ce/SrFeO₃ over that of 0.4Ce/SrFeO₃ in ethane ODH reaction (Fig. 3b). Using O_2 , instead of CO_2 to regenerate the reduced 0.2Ce/SrFeO₃ sample did significantly affect the distribution of active oxygen species. Specifically, a higher amount of active oxygen species can be attained upon O_2 oxidation in comparison to CO_2 regeneration (54.8% vs. 40.8%, Table S5). Nevertheless, over 40% of the O_2 -regenerated active oxygen was electrophilic oxygen species, while it was only 12% for the CO_2 -regenerated sample. This explains well the high CO_2 selectivity attained by 0.2Ce/SrFeO₃ (O_2) in ethane ODH reaction (Fig. 3b and Fig. S2e).

4.3. O_2 -TPD and H_2 -TPR

To characterize the relative amount of adsorbed and lattice oxygen species, O_2 -TPD test was performed over the three samples of SrFeO_3 (1200 °C), 0.2Ce/SrFeO₃, and 0.2Ce/SrFeO₃ (O_2). Fig. 7a shows the O_2 -TPD profiles of the samples, and the intensities of signals are normalized on the basis of $\text{SrFeO}_{3-\delta}$ content. As is shown in Fig. 7a, there is a large peak observed at about 700 °C for the sample of 0.2Ce/SrFeO₃ (O_2). This peak can be associated with “weak-bonded” surface oxygen species. While for the two CO_2 -regenerated samples, i.e., SrFeO_3 (1200 °C) and 0.2Ce/SrFeO₃, such a peak was not shown up within the testing temperature range, indicating the significantly suppressed O_2 release property. These results agreed well with XPS observations shown above. Furthermore, the weak-bonded surface oxygen species usually led to deep oxidations [37,38]. This was also reflected by the worst ethylene selectivity of 0.2Ce/SrFeO₃ (O_2) in ethane ODH reaction.

H_2 -TPR test was further conducted to investigate the reducibility of the oxygen carrier. The signal intensity (also normalized on the basis of

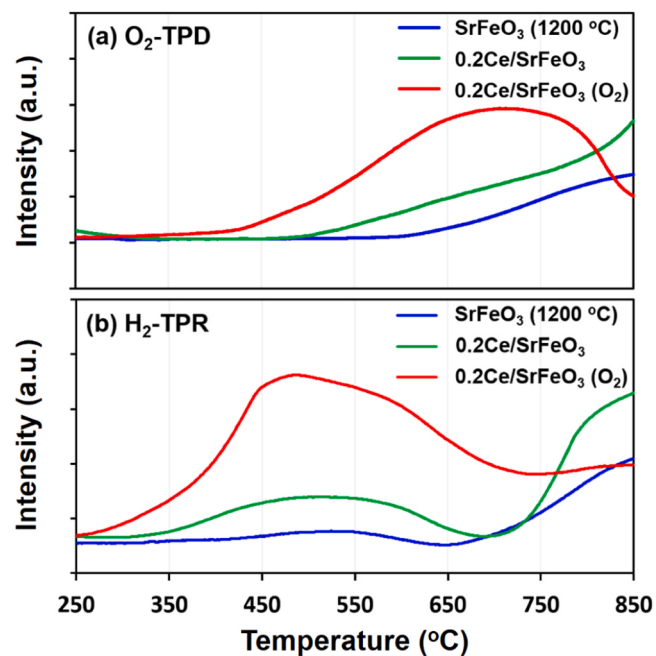


Fig. 7. (a) O_2 -TPD and (b) H_2 -TPR results of SrFeO_3 (1200 °C), 0.2Ce/SrFeO₃, and 0.2Ce/SrFeO₃ (O_2). Temperature range, 250–850 °C; ramping rate, 5 °C/min; gas stream, 60 mL/min of pure Ar in O_2 -TPD and 60 mL/min of 5 vol.% H_2 /Ar in H_2 -TPR. Notes: the sample of SrFeO_3 (1200 °C) was calcined at 1200 °C for 12 h, while all the others were calcined at 850 °C for 4 h; the 0.2Ce/SrFeO₃ (O_2) was regenerated by O_2 , while all the others were by CO_2 .

$\text{SrFeO}_{3-\delta}$ content) of H_2 -TPR profiles for each sample is shown in Fig. 7b. As it can be seen, two main reduction peaks can be observed for all samples, locating at 470–540 °C and above 850 °C, respectively. Among the three samples, the corresponding temperatures of the initial reduction peak position follow the sequence of 0.2Ce/SrFeO₃ (O_2) < 0.2Ce/SrFeO₃ < SrFeO_3 (1200 °C), while the sequence order in peak intensity is just the opposite. These results clearly suggest that the addition of Ce increases the reducibility of $\text{SrFeO}_{3-\delta}$, while CO_2 regeneration significantly decreases the reducibility of the sample as compared to O_2 regeneration. Generally, a higher sample reducibility corresponds to higher ODH activity [37]. This was also indicated by the ethane ODH reaction data shown in Fig. 3b.

4.4. Density functional theory (DFT) calculation

The underlying mechanism for the enhanced activity of Ce-modified $\text{SrFeO}_{3-\delta}$ was explored through DFT calculation. The oxygen vacancy of oxygen carrier was considered to exhibit a pivotal role in ODH reactions [57,58]. Therefore, the effect of Ce addition on the oxygen vacancy formation of the surface slab was investigated, as shown in Fig. 8. We note here that, XRD results indicated the co-existence of CeO_2 and potential Ce substitution of $\text{SrFeO}_{3-\delta}$ for Ce-modified samples, thus both CeO_2 cluster (Fig. 8b) and Ce-substituted SrFeO_3 (Fig. 8c) were considered in DFT model construction. As indicated by the computation results, the surface oxygen vacancy formation energy (E_{ov}) on the SrFeO_3 substrate (2.386 eV) decreased obviously upon Ce modification, as attained as 2.02 eV and 1.93 eV for CeO_2 adsorbed SrFeO_3 and Ce-substituted SrFeO_3 , respectively. Such findings suggest improved surface oxygen activity of the SrFeO_3 substrate after Ce modification, which is therefore beneficial to facilitate ethane conversion in ODH reaction. This was consistent with experimental results. Moreover, the surface oxygen activity of CeO_2 cluster is relatively poor in comparison with that of SrFeO_3 substrate, as indicated by the much higher oxygen vacancy formation energy of CeO_2 cluster (2.465 eV). From this perspective, too much of Ce addition to $\text{SrFeO}_{3-\delta}$ would be

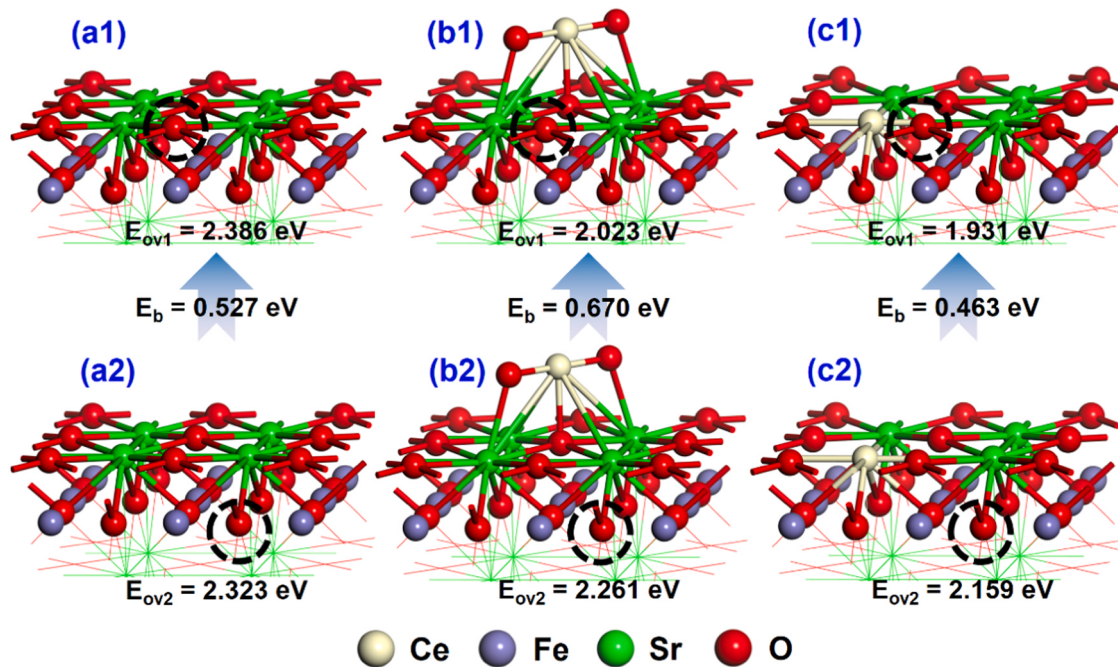


Fig. 8. The oxygen vacancy formation energy (E_{ov}) and oxygen diffusion energy barrier (E_b) on the (a) SrFeO_3 substrate; (b) CeO_2 adsorbed SrFeO_3 substrate; (c) partial Ce-substituted SrFeO_3 substrate. E_{ov1} and E_{ov2} represents the surface oxygen vacancy formation energy and subsurface oxygen vacancy formation energy, respectively. Notes: The O atom marked by the black dotted circle indicates that it has been removed.

disadvantageous to the overall activity of the oxygen carrier, which can also be confirmed by the higher activity of $0.2\text{Ce}/\text{SrFeO}_3$ than that of $0.4\text{Ce}/\text{SrFeO}_3$ in ODH reaction.

As known, the capability of oxygen diffusion from the bulk to the surface is highly related to the selectivity of the oxygen carrier in ODH reactions, in which a lower oxygen diffusion capability is generally beneficial for ethylene generation [37,38]. The energy barriers of oxygen diffusion (E_b) from the subsurface layer to the surface layer for SrFeO_3 substrate, CeO_2 adsorbed SrFeO_3 , and Ce-substituted SrFeO_3 were further calculated, as 0.53 eV, 0.67 eV, and 0.46 eV shown in Fig. 8, respectively. To some extent, the calculation results agree with the higher ethylene selectivity of SrFeO_3 than that of Ce-modified samples in reaction.

Further simulations were conducted to reveal the reason for the significantly varied ethylene selectivity of the oxygen carriers regenerated by different oxidants (CO_2 or O_2). For the simulation, a defected Ce-substituted SrFeO_3 slab model with an oxygen vacancy on the surface of the slab was constructed to represent the CO_2 -regenerated sample (Fig. S10), while the slab with perfect surface was used to represent the O_2 -regenerated sample (Fig. 8c). The energy barriers of lattice oxygen diffusion from the subsurface layer to the surface layer was calculated to determine the effect of the existence of surface oxygen vacancy on the lattice oxygen diffusion capability of the slab, as shown in Fig. S10 of Supporting information. As it turned out, the energy barrier of oxygen diffusion on the defected surface increased to 0.92 eV, which doubled as compared with that of the perfect surface. With this regard, it is no wonder that much higher ethylene selectivity was attained by $0.2\text{Ce}/\text{SrFeO}_3$ in ethane ODH reaction, when compared with that of $0.2\text{Ce}/\text{SrFeO}_3$ (O_2).

5. Conclusion

In this work, we demonstrated the scheme of ethane oxidative dehydrogenation (ODH) coupled with CO_2 splitting in a chemical looping manner using Ce-modified $\text{SrFeO}_{3-\delta}$ as oxygen carrier. The introduction of Ce was found to facilitate the formation of $\text{SrFeO}_{3-\delta}$ perovskite phase under much “milder” calcination conditions, as

compared to the sample without Ce modification. In addition, improved activity towards ethane conversion in the ODH step as well as higher CO generation in the subsequent CO_2 splitting step were observed over Ce-modified $\text{SrFeO}_{3-\delta}$ samples. Through a total of 39 redox cycles, the sample of $0.2\text{Ce}/\text{SrFeO}_3$ achieved a stable ethylene yield of 23.8% at 725 °C and 3000 h⁻¹, which was over twice as that of thermal blank. In the meantime, the CO generation was attained as 0.25 mmol/g in the CO_2 splitting step, at a peak CO_2 conversion of 69.4%. Regenerating the reduced $0.2\text{Ce}/\text{SrFeO}_3$ sample with O_2 instead of CO_2 was found to significantly decrease the ethylene selectivity of the re-oxidized sample, due to the higher proportion of nonselective electrophilic oxygen species on the near-surface of the O_2 -regenerated sample. Characterizations including XRD, XPS, TEM-EDS, O_2 -TPD, H_2 -TPR, C_2H_6 -TPR, as well as density functional theory (DFT) calculation were used to probe the underlying mechanism of the varied reaction performance attained by different samples. As indicated, a proper amount of Ce addition tended to improve the activity of the sample by altering the $\text{Fe}^{2+}/(\text{Fe}^{3+}+\text{Fe}^{4+})$ ratio and the amount of active oxygen species on the near-surface of the particle. H_2 -TPR testing results further confirmed the improved reducibility of Ce-modified samples. DFT calculation results showed that the enhanced activity of Ce-modified samples was due to the decrease in surface oxygen vacancy formation energy of the $\text{SrFeO}_{3-\delta}$ substrate. The better ODH reaction performance of the CO_2 -regenerated sample was attributed to the obvious increase in lattice oxygen diffusion resistance as compared with that of O_2 regeneration. All these findings can provide useful guidance for the development of appropriate oxygen carrier for the coupled ethane ODH and CO_2 splitting process. In future work, it is necessary to further improve the in situ H_2 combustion capability of the oxygen carrier in the ethane ODH step, so as to facilitate CO_2 conversion as well as CO generation in the subsequent CO_2 splitting step.

Supporting information

Details on data evaluation (including ethane conversion, selectivity, yield, and H_2 conversion in the ethane ODH step, as well as CO_2 conversion and CO generation in the CO_2 splitting step); expanded reaction data for oxygen carriers as well as thermal blank; redox cycling testing

results of 0.2Ce/SrFeO₃; BET, XRD, XPS, and TEM-EDS results of the oxygen carriers; DFT calculation details and results.

CRediT authorship Contribution Statement

Xin Tian: Conceptualization, Methodology, Investigation, Reaction tests, Characterization, Draft Writing and editing, Funding acquisition. **Chaohe Zheng:** DFT calculation, Draft review and editing. **Haibo Zhao:** Supervision, Draft review and editing, Funding acquisition.

Declaration of Competing Interest

The authors declare that they have no known competing financial interests or personal relationships that could have appeared to influence the work reported in this paper.

Acknowledgments

This work was supported by the National Natural Science Foundation of China (51906076, 51920105009, 52025063), and the China Postdoctoral Science Foundation (2019M662619, 2020T130219). We also acknowledge the financial supports from Guangdong Provincial Key Laboratory of New and Renewable Energy Research and Development (E039kf0401) and Foundation of State Key Laboratory of High-efficiency Utilization of Coal and Green Chemical Engineering (2021-K38).

Appendix A. Supporting information

Supplementary data associated with this article can be found in the online version at [doi:10.1016/j.apcatb.2021.120894](https://doi.org/10.1016/j.apcatb.2021.120894).

References

- [1] R.D. Vidic, S.L. Brantley, J.M. Vandenbossche, D. Yoxtheimer, J.D. Abad, Impact of shale gas development on regional water quality, *Science* 340 (2013) 6134.
- [2] B. Yan, S. Yao, S. Kattel, Q. Wu, Z. Xie, E. Gomez, P. Liu, D. Su, J.G. Chen, Active sites for tandem reactions of CO₂ reduction and ethane dehydrogenation, *Proc. Natl. Acad. Sci.* 115 (2018) 8278–8283.
- [3] R. Zhang, H. Wang, S. Tang, C. Liu, F. Dong, H. Yue, B. Liang, Photocatalytic oxidative dehydrogenation of ethane using CO₂ as a soft oxidant over Pd/TiO₂ catalysts to C₂H₄ and syngas, *ACS Catal.* 8 (2018) 9280–9286.
- [4] J.J. Sattler, J. Ruiz-Martinez, E. Santillan-Jimenez, B.M. Weckhuysen, Catalytic dehydrogenation of light alkanes on metals and metal oxides, *Chem. Rev.* 114 (2014) 10613–10653.
- [5] D. Dogu, K.E. Meyer, A. Fuller, S. Gunduz, D.J. Deka, N. Kramer, A.C. Co, U. S. Ozkan, Effect of lanthanum and chlorine doping on strontium titanates for the electrocatalytically-assisted oxidative dehydrogenation of ethane, *Appl. Catal. B: Environ.* 227 (2018) 90–101.
- [6] L. Shi, Y. Wang, B. Yan, W. Song, D. Shao, A.-H. Lu, Progress in selective oxidative dehydrogenation of light alkanes to olefins promoted by boron nitride catalysts, *Chem. Commun.* 54 (2018) 10936–10946.
- [7] Y.S. Yun, M. Lee, J. Sung, D. Yun, T.Y. Kim, H. Park, K.R. Lee, C.K. Song, Y. Kim, J. Lee, Y.-J. Seo, I.K. Song, J. Yi, Promoting effect of cerium on MoVTeNb mixed oxide catalyst for oxidative dehydrogenation of ethane to ethylene, *Appl. Catal. B: Environ.* 237 (2018) 554–562.
- [8] M.A. Atanga, F. Rezaei, A. Jawad, M. Fitch, A.A. Rownaghi, Oxidative dehydrogenation of propane to propylene with carbon dioxide, *Appl. Catal. B: Environ.* 220 (2018) 429–445.
- [9] B. Sarkar, R. Goyal, L.N. Sivakumar Konathala, C. Pendem, T. Sasaki, R. Bal, MoO₃ nanoclusters decorated on TiO₂ nanorods for oxidative dehydrogenation of ethane to ethylene, *Appl. Catal. B: Environ.* 217 (2017) 637–649.
- [10] F. Cavani, N. Ballarini, A. Cericola, Oxidative dehydrogenation of ethane and propane: how far from commercial implementation? *Catal. Today* 127 (2007) 113–131.
- [11] C.A. Gärtnner, A.C. vanVeen, J.A. Lercher, Oxidative dehydrogenation of ethane: common principles and mechanistic aspects, *ChemCatChem* 5 (2013) 3196–3217.
- [12] V.P. Haribal, L.M. Neal, F. Li, Oxidative dehydrogenation of ethane under a cyclic redox scheme – process simulations and analysis, *Energy* 119 (2017) 1024–1035.
- [13] R. Koifala, R. Buechel, F. Krumeich, S.E. Pratsinis, A. Baiker, Oxidative dehydrogenation of ethane with CO₂ over flame-made Ga-loaded TiO₂, *ACS Catal.* 5 (2015) 690–702.
- [14] A. Tóth, G. Halasi, F. Solymosi, Reactions of ethane with CO₂ over supported Au, *J. Catal.* 330 (2015) 1–5.
- [15] M. Myint, B. Yan, J. Wan, S. Zhao, J.G. Chen, Reforming and oxidative dehydrogenation of ethane with CO₂ as a soft oxidant over bimetallic catalysts, *J. Catal.* 343 (2016) 168–177.
- [16] S. Wang, Z.H. Zhu, Catalytic conversion of alkanes to olefins by carbon dioxide oxidative dehydrogenation: a review, *Energy Fuels* 18 (2004) 1126–1139.
- [17] G. Li, C. Liu, X. Cui, Y. Yang, F. Shi, Oxidative dehydrogenation of light alkanes with carbon dioxide, *Green. Chem.* 23 (2021) 689–707.
- [18] E. Gomez, X. Nie, J.H. Lee, Z. Xie, J.G. Chen, Tandem reactions of CO₂ reduction and ethane aromatization, *J. Am. Chem. Soc.* 141 (2019) 17771–17782.
- [19] A. Al-Mamoori, S. Lawson, A.A. Rownaghi, F. Rezaei, Oxidative dehydrogenation of ethane to ethylene in an integrated CO₂ capture-utilization process, *Appl. Catal. B: Environ.* 278 (2020), 119329.
- [20] J. Liu, Y. Gao, X. Wang, F. Li, Molten-salt-mediated carbon dioxide capture and superequilibrium utilization with ethane oxidative dehydrogenation, *Cell Rep. Phys. Sci.* 2 (2021), 100503.
- [21] J. Adanez, A. Abad, F. Garcia-Labiano, P. Gayan, L.F. de Diego, Progress in chemical-looping combustion and reforming technologies, *Prog. Energy Combust. Sci.* 38 (2012) 215–282.
- [22] X. Zhu, Q. Imitiaz, F. Donat, C.R. Müller, F. Li, Chemical looping beyond combustion—a perspective, *Energy Environ. Sci.* 13 (2020) 772–804.
- [23] D. Zeng, Y. Qiu, L. Ma, M. Li, D. Cui, S. Zhang, R. Xiao, Tuning the support properties toward higher CO₂ conversion during a chemical looping scheme, *Environ. Sci. Technol.* 54 (2020) 12467–12475.
- [24] Y. Qiu, L. Ma, M. Li, D. Cui, S. Zhang, D. Zeng, R. Xiao, Copper and cobalt co-doped ferrites as effective agents for chemical looping CO₂ splitting, *Chem. Eng. J.* 387 (2020), 124150.
- [25] M.H. Jeong, J. Sun, G. Young Han, D.H. Lee, J.W. Bae, Successive reduction-oxidation activity of FeO_x/TiO₂ for dehydrogenation of ethane and subsequent CO₂ activation, *Appl. Catal. B: Environ.* 270 (2020), 118887.
- [26] N.Y. Usachev, I.M. Gerzeliev, V.V. Kharlamov, V.P. Kalinin, E.P. Belanova, S. A. Kanaev, A.V. Kazakov, T.S. Starostina, Oxidative conversion of ethane involving lattice oxygen of molybdenum systems modified with aluminum, gallium, or yttrium oxide, *Pet. Chem.* 56 (2016) 841–845.
- [27] A.H. Elbadawi, M.S. Ba-Shammakh, S. Al-Ghamdi, S.A. Razzak, M.M. Hossain, H. I. de Lasa, A fluidizable VO_x/ γ -Al₂O₃-ZrO₂ catalyst for the ODH of ethane to ethylene operating in a gas phase oxygen free environment, *Chem. Eng. Sci.* 145 (2016) 59–70.
- [28] L.M. Neal, S. Yusuf, J.A. Sofranko, F. Li, Oxidative dehydrogenation of ethane: a chemical looping approach, *Energy Technol.* 4 (2016) 1200–1208.
- [29] R.B. Dudek, X. Tian, M. Blivin, L.M. Neal, H. Zhao, F. Li, Perovskite oxides for redox oxidative cracking of n-hexane under a cyclic redox scheme, *Appl. Catal. B: Environ.* 246 (2019) 30–40.
- [30] Y. Gao, L. Neal, D. Ding, W. Wu, C. Baroi, A.M. Gaffney, F. Li, Recent advances in intensified ethylene production—a review, *ACS Catal.* 9 (2019) 8592–8621.
- [31] W. Ding, K. Zhao, S. Jiang, Z. Zhao, Y. Cao, F. He, Alkali-metal enhanced LaMnO₃ perovskite oxides for chemical looping oxidative dehydrogenation of ethane, *Appl. Catal. A: Gen.* 609 (2021), 117910.
- [32] S. Yusuf, L.M. Neal, F. Li, Effect of promoters on manganese-containing mixed metal oxides for oxidative dehydrogenation of ethane via a cyclic redox scheme, *ACS Catal.* 7 (2017) 5163–5173.
- [33] S. Yusuf, L. Neal, V. Haribal, M. Baldwin, H.H. Lamb, F. Li, Manganese silicate based redox catalysts for greener ethylene production via chemical looping – oxidative dehydrogenation of ethane, *Appl. Catal. B: Environ.* 232 (2018) 77–85.
- [34] S. Yusuf, V. Haribal, D. Jackson, L. Neal, F. Li, Mixed iron-manganese oxides as redox catalysts for chemical looping-oxidative dehydrogenation of ethane with tailororable heat of reactions, *Appl. Catal. B: Environ.* 257 (2019), 117885.
- [35] S. Yusuf, L. Neal, Z. Bao, Z. Wu, F. Li, Effects of sodium and tungsten promoters on Mg₆MnO₈-based core-shell redox catalysts for chemical looping—oxidative dehydrogenation of ethane, *ACS Catal.* 9 (2019) 3174–3186.
- [36] X. Tian, C. Zheng, F. Li, H. Zhao, Co and Mo Co-doped Fe₂O₃ for selective ethylene production via chemical looping oxidative dehydrogenation, *ACS Sustain. Chem. Eng.* 9 (2021) 8002–8011.
- [37] Y. Gao, L.M. Neal, F. Li, Li-Promoted La_xSr_{2-x}FeO_{4-δ} core–shell redox catalysts for oxidative dehydrogenation of ethane under a cyclic redox scheme, *ACS Catal.* 6 (2016) 7293–7302.
- [38] Y. Gao, F. Haeri, F. He, F. Li, Alkali metal-promoted La_xSr_{2-x}FeO_{4-δ} redox catalysts for chemical looping oxidative dehydrogenation of ethane, *ACS Catal.* 8 (2018) 1757–1766.
- [39] Y. Gao, X. Wang, J. Liu, C. Huang, K. Zhao, Z. Zhao, X. Wang, F. Li, A molten carbonate shell modified perovskite redox catalyst for anaerobic oxidative dehydrogenation of ethane, *Sci. Adv.* 6 (2020) eaaz9339.
- [40] P. Novotný, S. Yusuf, F. Li, H.H. Lamb, Oxidative dehydrogenation of ethane using MoO₃/Fe₂O₃ catalysts in a cyclic redox mode, *Catal. Today* 317 (2018) 50–55.
- [41] R.X. Valenzuela, G. Bueno, V. Corberán, Y. Xu, C. Chen, Selective oxidehydrogenation of ethane with CO₂ over CeO₂-based catalysts, *Catal. Today* 61 (2000) 43–48.
- [42] R.X. Valenzuela, G. Bueno, A. Solbes, F. Sapiña, E. Martínez, V. Corberán, Nanostructured ceria-based catalysts for oxydehydrogenation of ethane with CO₂, *Top. Catal.* 15 (2001) 181–188.
- [43] T.D. Nguyen, W. Zheng, F.E. Celik, G. Tsilomelekis, CO₂-assisted ethane oxidative dehydrogenation over MoO_x catalysts supported on reducible CeO₂-TiO₂, *Catalysis 11* (2021) 5791–5801.
- [44] Y. Li, L. Li, W. Sun, C. Chen, S. Luo, J. Shen, C. Jiang, F. Jing, Porous silica coated ceria as a switch in tandem oxidative dehydrogenation and dry reforming of ethane with CO₂, *ChemCatChem* 13 (2021) 3501–3509.

- [45] X. Tian, M. Su, H. Zhao, Kinetics of redox reactions of CuO@TiO₂-Al₂O₃ for chemical looping combustion and chemical looping with oxygen uncoupling, *Cambust. Flame* 213 (2020) 255–267.
- [46] J.P. Perdew, J.A. Chevary, S.H. Vosko, K.A. Jackson, M.R. Pederson, D.J. Singh, C. Fiolhais, Atoms, molecules, solids, and surfaces: applications of the generalized gradient approximation for exchange and correlation, *Phys. Rev. B* 46 (1992) 6671–6687.
- [47] J.P. Hedges, S. Short, J.D. Jorgensen, X. Xiong, B. Dabrowski, S.M. Mini, C. W. Kimball, Evolution of oxygen-vacancy ordered crystal structures in the Perovskite series Sr_nFe_nO_{3n-1} ($n=2, 4, 8$, and ∞), and the relationship to electronic and magnetic properties, *J. Solid State Chem.* 151 (2000) 190–209.
- [48] A. Takamatsu, K. Tamai, S. Hosokawa, T. Tanaka, M. Ehara, R. Fukuda, Oxidation and storage mechanisms for nitrogen oxides on variously terminated (001) surfaces of SrFeO_{3-δ} and Sr₃Fe₂O_{7-δ} Perovskites, *ACS Appl. Mater. Interfaces* 13 (2021) 7216–7226.
- [49] Y. Zhang, E. Cao, L. Sun, J. Hu, Adsorption of NO on the SrFeO₃ (001) surface: a DFT study, *Comput. Mater. Sci.* 102 (2015) 135–139.
- [50] B. Li, S. He, J. Li, X. Yue, J.T.S. Irvine, D. Xie, J. Ni, C. Ni, A Ce/Ru codoped SrFeO_{3-δ} Perovskite for a coke-resistant anode of a symmetrical solid oxide fuel cell, *ACS Catal.* 10 (2020) 14398–14409.
- [51] F. Deganello, L.F. Liotta, A. Longo, M.P. Casaleotto, M. Scopelliti, Cerium effect on the phase structure, phase stability and redox properties of Ce-doped strontium ferrates, *J. Solid State Chem.* 179 (2006) 3406–3419.
- [52] E.J. Marek, E. García-Calvo Conde, Effect of catalyst preparation and storage on chemical looping epoxidation of ethylene, *Chem. Eng. J.* 417 (2021), 127981.
- [53] T. Blasco, J.M.L. Nieto, Oxidative dyhydrogenation of short chain alkanes on supported vanadium oxide catalysts, *Appl. Catal. A: Gen.* 157 (1997) 117–142.
- [54] W. Fan, Z. Sun, Y. Bai, K. Wu, Y. Cheng, Highly stable and efficient Perovskite ferrite electrode for symmetrical Solid oxide fuel cells, *ACS Appl. Mater. Interfaces* 11 (2019) 23168–23179.
- [55] N.A. Merino, B.P. Barbero, P. Eloy, L.E. Cadús, La_{1-x}Ca_xCoO₃ perovskite-type oxides: identification of the surface oxygen species by XPS, *Appl. Surf. Sci.* 253 (2006) 1489–1493.
- [56] C. Li, W. Wang, N. Zhao, Y. Liu, B. He, F. Hu, C. Chen, Structure properties and catalytic performance in methane combustion of double perovskites Sr₂Mg_{1-x}Mn_xMoO_{6-δ}, *Appl. Catal. B: Environ.* 102 (2011) 78–84.
- [57] S. Chen, L. Zeng, R. Mu, C. Xiong, Z.-J. Zhao, C. Zhao, C. Pei, L. Peng, J. Luo, L.-S. Fan, J. Gong, Modulating lattice oxygen in dual-functional Mo-V-O mixed oxides for chemical looping oxidative dehydrogenation, *J. Am. Chem. Soc.* 141 (2019) 18653–18657.
- [58] S. Chen, C. Pei, X. Chang, Z.-J. Zhao, R. Mu, Y. Xu, J. Gong, Coverage-dependent behaviors of vanadium oxides for chemical looping oxidative dehydrogenation, *Angew. Chem. Int. Ed.* 59 (2020) 22072–22079.